RESEARCH ARTICLE

ADVANCED MATERIALS
www.advmat.de

Direct Visualization of Defect-Controlled Diffusion in van der Waals Gaps

Joachim Dahl Thomsen, Yaxian Wang, Henrik Flyvbjerg, Eugene Park, Kenji Watanabe, Takashi Taniguchi, Prineha Narang,* and Frances M. Ross**

Diffusion processes govern fundamental phenomena such as phase transformations, doping, and intercalation in van der Waals (vdW) bonded materials. Here, the diffusion dynamics of W atoms by visualizing the motion of individual atoms at three different vdW interfaces: hexagonal boron nitride (BN)/vacuum, BN/BN, and BN/WSe$_2$, by recording scanning transmission electron microscopy movies is quantified. Supported by density functional theory (DFT) calculations, it is inferred that in all cases diffusion is governed by intermittent trapping at electron beam-generated defect sites. This leads to diffusion properties that depend strongly on the number of defects. These results suggest that diffusion and intercalation processes in vdW materials are highly tunable and sensitive to crystal quality. The demonstration of imaging, with high spatial and temporal resolution, of layers and individual atoms inside vdW heterostructures offers possibilities for direct visualization of diffusion and atomic interactions, as well as for experiments exploring atomic structures, their in situ modification, and electrical property measurements of active devices combined with atomic resolution imaging.

1. Introduction

Diffusion of atomic species in and on 2D materials governs numerous phenomena such as phase transformations,[1] crystal growth,[2] and doping.[3,4] In particular, the diffusion of foreign atoms into van der Waals (vdW) bonded materials to form intercalated structures has great potential for tuning physical properties (electronic, optoelectronic, magnetic), and for uses in energy storage and catalysis.[5,6]

Of particular interest, yet not widely studied, is diffusion within assembled vdW heterostructures. Such structures, consisting of stacked multilayer blocks of 2D crystals, form the basis for fundamental studies of the electrical properties and physics of 2D materials and devices. Most importantly, 2D materials encapsulated by hexagonal boron nitride (BN) are the de facto standard for creating devices with high-quality electrical properties;[7] stacked heterostructures show promise for novel electronic, optoelectronic,[8,9] magnetic devices,[10,11] and for exploring phenomena such as strongly correlated electron physics.[12] A microscopic understanding of diffusion pathways and dynamics in vdW heterostructures, including the role of defects, is important in providing opportunities for tailoring the properties of these structures. Measurements of diffusion in such heterostructures also offer advantages compared to studies of atomic motion on surfaces, since surface contamination issues are avoided and the diffusion environment can be well-controlled by trapping diffusing atoms between particular layers within the structure. For such

---

J. D. Thomsen, P. Narang
Division of Physical Sciences
College of Letters and Science
University of California
Los Angeles CL 90095, USA
E-mail: j.thomsen@fz-juelich.de; prineha@ucla.edu

J. D. Thomsen, E. Park, F. M. Ross
Department of Materials Science and Engineering
Massachusetts Institute of Technology
Cambridge, MA 02139, USA
E-mail: fmross@mit.edu

The ORCID identification number(s) for the author(s) of this article can be found under https://doi.org/10.1002/adma.202403989

DOI: 10.1002/adma.202403989

Y. Wang
Beijing National Laboratory for Condensed Matter Physics and Institute of Physics
Chinese Academy of Sciences
Beijing 100190, China

H. Flyvbjerg
Mark Kac Center for Complex Systems Research
Jagiellonian University
Kraków, Poland

K. Watanabe
Research Center for Electronic and Optical Materials
National Institute for Materials Science
1-1 Namiki, Tsukuba 305-0044, Japan

T. Taniguchi
Research Center for Materials Nanoarchitectonics
National Institute for Materials Science
1-1 Namiki, Tsukuba 305-0044, Japan

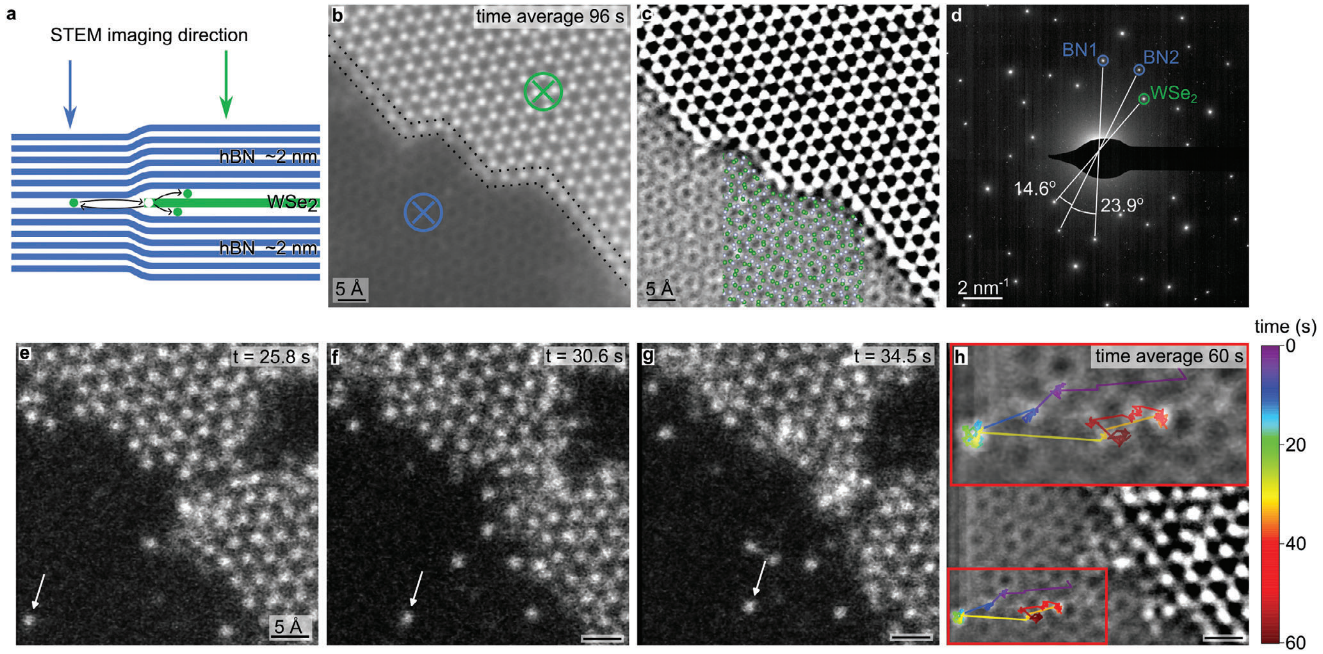

Figure 1. **Sample overview.** a) Cross-sectional sample schematic: Monolayer WSe_2 encapsulated within ≈2 nm thick BN on both sides. b) Sum of over 400 drift-corrected STEM-HAADF images at the WSe_2 edge from Video S1 (Supporting Information). The blue and green arrow tails indicate the same positions as shown by the arrows in (a). c) Same as (b) but with its own Gaussian blurred (15 pixel radius) version subtracted in order to emphasize the BN/BN moiré. An atomic model of twisted bilayer BN is shown on top of the BN/BN moiré. d) Diffraction pattern of the sample. The blue and green circles indicate a $\{11\bar{2}0\}$ spot from BN and WSe_2, respectively. The white solid lines indicate the twist angles between the different layers. e–g) Selected images from Video S2 (Supporting Information). The white arrows point to an atom tracked at the BN/BN interface. Scale bars are 5 Å. h) Time-averaged image. The trajectory of the tracked atom is shown on top of the image. The inset shows an enlarged image of the trajectory.

studies, TEM is a powerful tool with possibilities for real-time, atomic resolution imaging of diffusion processes, and has been used to image and quantify the diffusion of adsorbed or substitutional atoms on the surface of different 2D materials,[13–16] diffusion of dopants in a bulk semiconducting crystal,[17] and the motion of noble gas clusters ion-implanted into bilayer graphene.[18]

Here, we directly visualize the atomic scale dynamics of W diffusion inside a vdW heterostructure, at the interfaces between hexagonal boron nitride (BN)/BN, BN/WSe_2, and BN/vacuum. We show that the diffusion properties are governed by defects at the interfaces, which are created continuously by the electron beam, and which create trapping sites for W atoms. This leads to diffusion properties that are more affected by defect densities than the details of the interface structure such as the size of the vdW gap. We show that it is possible to span the range from an intrinsic regime with very few defects to a highly defective regime where W atoms undergo small displacements between defect sites.

The ability to image the dynamics of atoms embedded inside vdW heterostructures with high spatial and temporal resolution that we demonstrate here offers opportunities for quantifying diffusion processes and observing atomic interactions directly. The precise identification of different atomic species and their beam-controlled motion may even be possible.[19,20] Furthermore, our high-resolution imaging of individual atoms within BN-encapsulated heterostructures suggests that it may be possible to combine electrical and structural measurements of the active material in a vdW device through appropriate experimental design.

2. Atomic Motion in the Van Der Waals Gap

To study the atomic motion of W atoms at vdW-bonded interfaces, we fabricated BN/WSe_2/BN heterolayer stacks with monolayer WSe_2 and ≈2 nm thick BN, i.e., ≈6 monolayers of BN. Details of sample fabrication are described in Experimental Section. By choosing WSe_2 crystals that were laterally smaller than the BN crystals, we embedded an edge of WSe_2 within the heterostructure. This served as the source of W (and Se) atoms, as discussed below. A schematic of this BN/WSe_2/BN heterostructure is shown in **Figure** 1a. Optical microscopy images of the samples are given in Figures S1 and S2 (Supporting Information). Such samples allow us to make quantitative comparisons between the diffusion of W atoms at the BN/WSe_2 and BN/BN interfaces. We measure diffusion at the BN/vacuum interface by creating simpler BN/WSe_2 heterostructures, consisting of ≈2 nm thick BN partially covered with monolayer WSe_2.

Figure 1a showed the ideal situation with pristine interfaces. In reality, during assembly of vdW heterostructures it is possible to form bubbles between the layers with trapped hydrocarbon contamination.[21–25] However, optical images of our heterostructure samples do not reveal visible bubbles on the regions containing monolayer WSe_2. Some bubbles in regions with thicker BN are indicated in Figures S1 and S2 (Supporting Information), but these areas were not used for our experiments. The contamination within bubbles would in any case be seen in scanning transmission electron micropscopy (STEM) or transmission electron microscopy (TEM) imaging due to the added mass of the hydrocarbon, but are not visible in overview images of the samples (Figure S3, Supporting Information). Bubble-free regions typically form clean interfaces due to a squeeze-out effect that pushes contaminants away,[21,24] especially when prepared with dry transfer methods as used here. However, the interlayer gap may differ from the gap predicted from density functional theory (DFT) calculations if either material is susceptible to oxidation.[26] In particular, the BN/WSe$_2$ interlayer gap was found to be slightly larger than expectations from DFT calculations.[26] Since we also prepared samples at ambient conditions we would expect a similar interlayer spacing.

In our samples, the sensitivity of high-angle annular dark field (HAADF)-STEM for heavier atoms allows us to image the monolayer WSe$_2$ and individual diffusing W atoms at sub-0.1 nm resolution through the BN layers (Figure 1b,c; Video S1, Supporting Information). Although individual Se atoms were also mobile and visible within the sample, we tracked the motion of W atoms because they appear brighter in HAADF-STEM imaging, as contrast scales with atomic mass as $Z^{1.7}$.[27] The layers were not rotationally aligned during the stacking process, and the rotational misalignment of the three layers can be measured from diffraction, as in Figure 1d. We measure a rotation angle of 23.9° between the two BN crystals. In Figure 1c we have superimposed an atomic model of twisted bilayer BN rotated to 23.9° which matches with features in the image. We use fixed conditions (electron beam energy and current, dwell time, magnification, and number of pixels per image) for all data used to quantify diffusion dynamics (see Experimental Section for imaging conditions and data analysis). All data shown in the main text is obtained with an electron beam energy of 200 keV and we provide additional data obtained at 60 keV in the Supporting Information.

During imaging of these structures, we then locate mobile W atoms that originate from the WSe$_2$ lattice. They can either diffuse at the interface between the two BN crystals or at the interface between the WSe$_2$ and BN. Figure 1e–g shows images of a W atom diffusing at the BN/BN interface, see also Video S2 (Supporting Information). Figure 1h is an averaged image from the video with the trajectory of the W atom also shown. From such trajectories, we can study the atomic scale dynamics and statistics or the W atom motion at the different interfaces. These videos show atomic trajectories that resemble a diffusion process with intermittent trapping (Figure 1h),[28] where an atom makes displacements between distinct sites at which it resides for some time. We note that even with a frame time of 0.217 s, atoms remain at such sites for multiple frames. Thus the observations can capture the dynamics of atomic residence at certain sites, even if diffusion processes occur on a faster time scale where rapid jumps are likely not resolved.

In the following sections, we describe and analyze the formation of diffusing W atoms and W diffusion process at the atomic scale at the WSe$_2$/BN, BN/BN, and BN/vacuum interfaces.

3. Diffusion at the BN/WSe$_2$ Interface

We first discuss the origin of the moving W atoms at the BN/WSe$_2$ interface. Upon initially imaging a pristine BN/WSe$_2$/BN region, we observe that W ejection from the bulk WSe$_2$ is preceded consistently by the formation of neighboring single or double selenium vacancies (**Figure** 2a–c; Video S3, Supporting Information). Another example is given in Figure S4 (Supporting Information). This takes place on a timescale of ≈1 min. The knock-on threshold for W atoms in a pristine WSe$_2$ lattice is above 500 keV while the threshold for Se atoms is 190 keV.[29] The observation of Se vacancy formation as the first step of the process is therefore consistent with a beam-driven effect.

We have also observed W atoms at the edge of the WSe$_2$ lattice diffuse into the BN/WSe$_2$ interface (Video S4, Supporting Information). Figure 2g–k shows images with a moving W atom indicated by a white arrow. Figure 2l shows the trajectory of the atom.

After their release from the WSe$_2$ lattice, we track the diffusion behavior of single W atoms at the BN/WSe$_2$ interface. **Figure** 3a–d and Video S5 (Supporting Information) follows a W atom as it is ejected from the WSe$_2$ lattice and sits at different times in a Se$_2$ site (Figure 3a), a W site (Figure 3b), and a hexagonal or “hollow” (H) site (Figure 3c). It finally becomes reincorporated into the WSe$_2$ lattice (Figure 3d), albeit at a different location from its origin because the W vacancy diffused a distance of one unit cell, as shown in Figure 3c. Since the W atom can reincorporate into the WSe$_2$ lattice, this suggests that the W atoms diffuse directly at the BN/WSe$_2$ interface, and do not diffuse into another vdW gap. Figure 3e displays the total trajectory. See Figures S5 and S6 (Supporting Information) for trajectories of additional W atoms measured at the BN/WSe$_2$ interface. The data shown in Figure 3 and Figures S5 and S6 (Supporting Information) are consistent in that the W atoms reside on W and Se$_2$ sites at about the same rate, 41% and 40% of frames, respectively, while they reside on a H site on 19% of frames (Figure 3f, see Experimental Section for details).

We next compare the statistics in Figure 3f with expectations from DFT calculations (Experimental Section) to better understand the potential landscape experienced by the interstitial W atoms. We perform calculations of the BN/WSe$_2$ interface, for simplicity including only monolayer BN in the calculation. We do not expect the results to change if we include multiple BN layers, based on our calculations for the free surface of BN of different thicknesses (see “Diffusion at the BN/Vacuum Interface”). We find that the most stable site for an interstitial W atom in a pristine WSe$_2$/BN interface is directly beneath another W site (Figure 3g).

We then computationally introduce vacancies into the system, adding both N and B vacancies since both vacancy types could be present: B vacancies were considered more common during TEM imaging of BN,[30,31] although recent literature suggests that both the accelerating voltage and vacuum level could change the prevalence. Indeed, at 200 keV, N vacancies may be more prevalent than B vacancies.[32] Unsurprisingly, Se, B, and N vacancies (Figure 3h–j), respectively) are stable sites for the W atom, as it can form bonds to the three neighboring W, N, or B atoms, respectively. This does not depend on the location of the vacancy with respect to the moiré unit cell, as shown in Figure S7a (Supporting Information), where a W atom behaves similarly when the B vacancy is in a different location. Furthermore, DFT calculations indicate that B and N vacancies behave in a qualitatively similar manner. Since B and N sites can not be distinguished in

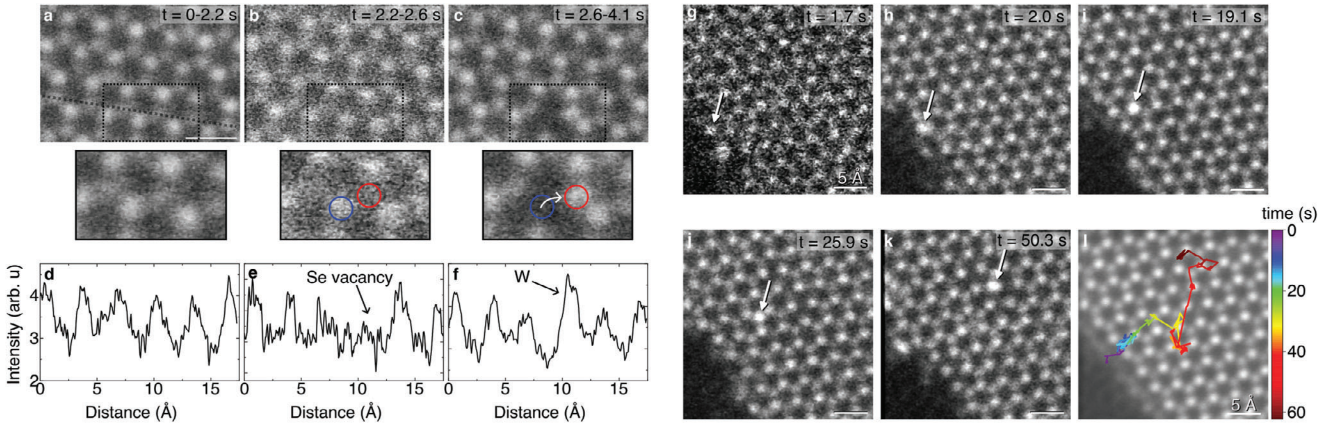

Figure 2. Creation of mobile W atoms. From the WSe_2 bulk: a–c) Data from Video S3 (Supporting Information) - STEM-HAADF images of a $BN/WSe_2/BN$ heterostructure. The insets show the region in the dashed rectangle. a) Sum of 10 subsequent frames, t=0–2.2 s. b) Sum of 2 frames, t=2.2–2.6 s. A Se vacancy has formed in the lattice site denoted by the red circle. The blue circle indicates the W atom that subsequently is ejected from the lattice. c) Sum of 7 frames showing the indicated W atom has moved to the Se vacancy site, t=2.6-4.1 s. d–f) Line profiles (5 pixel wide) along the dashed black line shown in (a). From the WSe_2 edge: g–k) Data from Video S4 (Supporting Information) - images of a tracked W atom (indicated by white arrows) that originated at the WSe_2 edge, and diffused at the BN/WSe_2 interface. l) Time-averaged image with the trajectory of the atom shown on top.

our experimental images, we discuss them together in the following analysis.

The interlayer distance appears to have only a small effect on the equilibrium position. In Figure S7b (Supporting Information) we compare the equilibrium position of a W atom in a N vacancy for the DFT-predicted interlayer spacing (as used in Figure 3j), and an experimentally determined interlayer spacing which is slightly larger.[26] The equilibrium positions differ only slightly (see Experimental Section for details) and we do not expect this small effect to impact our classification of resting sites given in Figure 3f.

If vacancies in the BN were to completely determine W pinning sites, then we would expect W atoms to reside equally on W, Se_2, and H sites since vacancies in the BN layers would be distributed above these sites equally. Since we find that W atoms reside mainly on W and Se sites, this indicates that the potential landscape of WSe_2 also plays a role in determining pinning sites. This is supported by previous calculations of Au diffusion in pristine heterostructures of graphene and transition metal dichalcogenides, where the calculated potential landscape predicted that diffusion pathways are along the W and Se_2 sites.[33] In our data, the equal prevalence of W and Se sites might further be due to the presence of Se vacancies, because in the pristine case the W site is preferred. Hence, analysis of the preferential resting sites for these interstitial atoms reveal that their motion is influenced by the presence of Se vacancies in the WSe_2 as well as B or N vacancies in the top and bottom BN layer. In the following, we will show that W diffusion at the BN/BN interface exhibits analogous characteristics.

4. Diffusion at the BN/BN Interface

Upon imaging a pristine BN/BN region near a WSe_2 edge, we find several mobile W atoms. We assume that these atoms are detached from the WSe_2 edge through interactions with the 200 kV electron beam because undercoordinated edge atoms are easier to eject. We find that the edge does not retract noticeably over extended periods of time (Figure 1b), but edge atoms detach and reattach analogous to a sublimation and deposition process on a surface. Only the outer row of atoms on the WSe_2 edge (highlighted in Figure 1b) appears blurry in the time-averaged-image (over 96 s) due to their motion.

To quantify the atomic scale details of W diffusion in the BN/BN interface, Figure 1e–h and **Figure** 4a–d show trajectories of W atoms at high magnification. See Figures S8 and S9 (Supporting Information) for trajectories of additional W atoms at the BN/BN interface. The atoms make several smaller displacements, <1 Å, seemingly around pinning sites, and fewer, larger displacements between such sites. We observe that the W atoms reside mainly on the moiré lattice of the BN/BN interface, i.e., on BN lattice sites. We compare this observation to DFT calculations for stable resting sites at the BN/BN interface. Figure 4e shows the model of the BN/BN interface that we used for these calculations (Experimental Section). The moiré unit cell features some distinctive sites that are indicated with blue circles and crosses in Figure 4e. The largest hollow space, denoted H_1, is present at the corners of the unit cell, while smaller hollow spaces are denoted by H_2 and H_3. Figure 4e shows that for a pristine BN/BN interface, the most stable site for the W atom is at H_1. This corresponds to the center of the "donut" shapes in Figure 4d (marked with a white cross). Configurations with W atoms at H_2 and H_3 display ≈200 meV higher energy than a configuration with a W atom at H_1 (Figure S7c,d, Supporting Information). However, introducing B vacancies at three distinct lattice sites on the moiré unit cell, namely the center (Ce), edge (E), and corner (Co) sites (Figure 4f–h) makes these sites significantly more stable positions for the W atoms. For example, in the case of an E site, the DFT calculations show that the total energy of the system increases by 7 eV when moving a W atom from E to H_1, see Figure S7e,f (Supporting Information), because 3 W–N bonds must be broken. This means that B vacancy sites are significantly more stable sites for W interstitials as compared to the "best" H_1 site in the pristine interface.

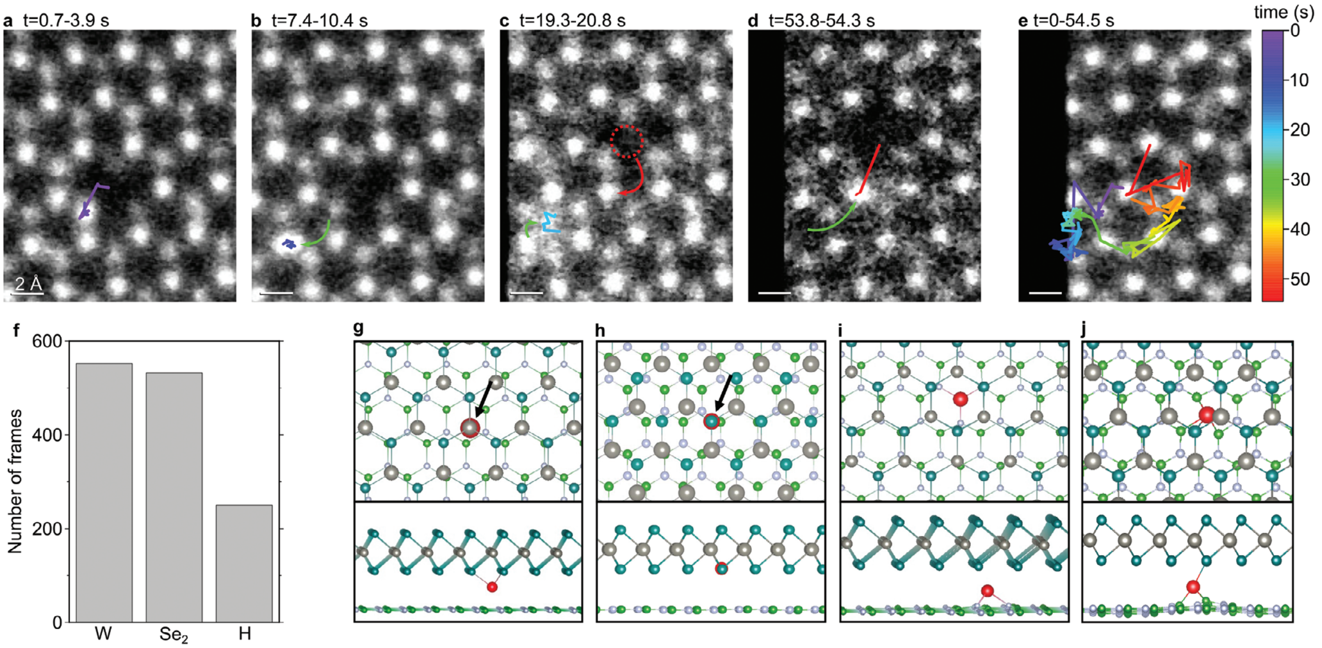

Figure 3. **Atomic motion at the BN/WSe$_2$ interface**. a–d) STEM-HAADF images obtained from Video S5 (Supporting Information) by summing the frames corresponding to the time interval indicated above each panel. Panels (a), (b), and (c) show snippets of the full trajectory, with the atom residing on a Se$_2$, W, and hollow site, respectively. Trajectories from the diffusing atom are overlaid to the images. In (a), the trajectory for t=0–3.9 s also shows the origin of the atom. In (d), the trajectory for t=53.8–54.5 s also includes the last recorded position where the atom reincorporates into the lattice. e) STEM-HAADF image was obtained by summing all frames in the video with tracks of the atom overlaid. f) Statistics of W resting sites obtained from the data shown in this figure as well as Figures S4 and S5 (Supporting Information). g–j) DFT-relaxed atomic structures. For computational simplicity, we have chosen to calculate a rotationally aligned BN/WSe$_2$ heterostructure, see Experimental Section for details. (g) The most stable position for W in a pristine BN/WSe$_2$ heterostructure. (h) The most stable position for W near a Se vacancy. i,j) Stable positions for W in the presence of a B and N vacancy, respectively. The different positions of W with respect to the WSe$_2$ layer illustrates that vacancies in the BN can greatly affect the preferred location of the W atom.

Overall, DFT simulations predict that the H$_1$ site should be the most stable resting site for W atoms in a pristine interface. However, we find experimentally that W atoms reside on the BN/BN moiré lattice in agreement with our DFT predictions that vacancies in the Ce, E, or Co sites are significantly more stable sites. These results therefore suggest that defects formed by the electron beam govern resting sites and diffusion properties at the BN/BN interface. This behavior is consistent with that seen for the BN/WSe$_2$ interface.

5. Diffusion at the BN/Vacuum Interface

We finally image W atoms on the free surface of ≈2 nm thick BN for comparison with the situations described above where the W atoms are encapsulated. For this experiment, we fabricate samples where monolayer WSe$_2$ is placed on a ≈2 nm thick BN crystal which is wider laterally than the WSe$_2$ crystal. Upon imaging the WSe$_2$ edge, we find several W atoms which have been released from the WSe$_2$ lattice and diffuse on the hBN surface.

Figure 5a,b displays the first and last images, respectively, from a video where we track one of these atoms. These images reveal that the WSe$_2$ edge recedes over time, with dislodged W/Se atoms aggregating in a structure on the edge that appears 3D, based on the proximity of the W atoms in projection. This behavior differs from the BN-encapsulated WSe$_2$ edge, where spatial confinement evidently prevents atoms on the WSe$_2$ edge from forming a 3D structure, so they instead detach and reattach in a 2D fashion (Figure 1a). Figure 5c shows an average of the entire video with the atom trajectory shown on top. We find that the atom makes several smaller displacements less than approximately an atomic spacing around a pinning site and fewer larger displacements over several atomic spacings in between such sites. Furthermore, we see that the pinning sites coincide with positions on the BN lattice.

Before performing a quantitative analysis of the observed motion, it is important to establish whether the W atoms in experiments such as that in Figure 5 are moving on the surface of the BN or between layers, as in Figure 4. Although we cannot measure the z-direction position from the images, several factors suggest the W atoms are on the surface. First, W atoms are released on the BN surface and the energetics of diffusion through a BN layer and into a vdW gap are unfavorable, even in the presence of beam-induced defects. Second, the analysis to be shown below yields consistent and different values for the diffusion coefficient in these experiments compared to those at the BN/BN interface; we attribute this to the presence of surface contamination.[34] Finally, in data such as Figure 3a–ea W atom is released from the WSe$_2$ lattice and later reincorporated. This particular atom therefore remained in the gap where it was released, showing that W atoms can make extended movements without changing planes.

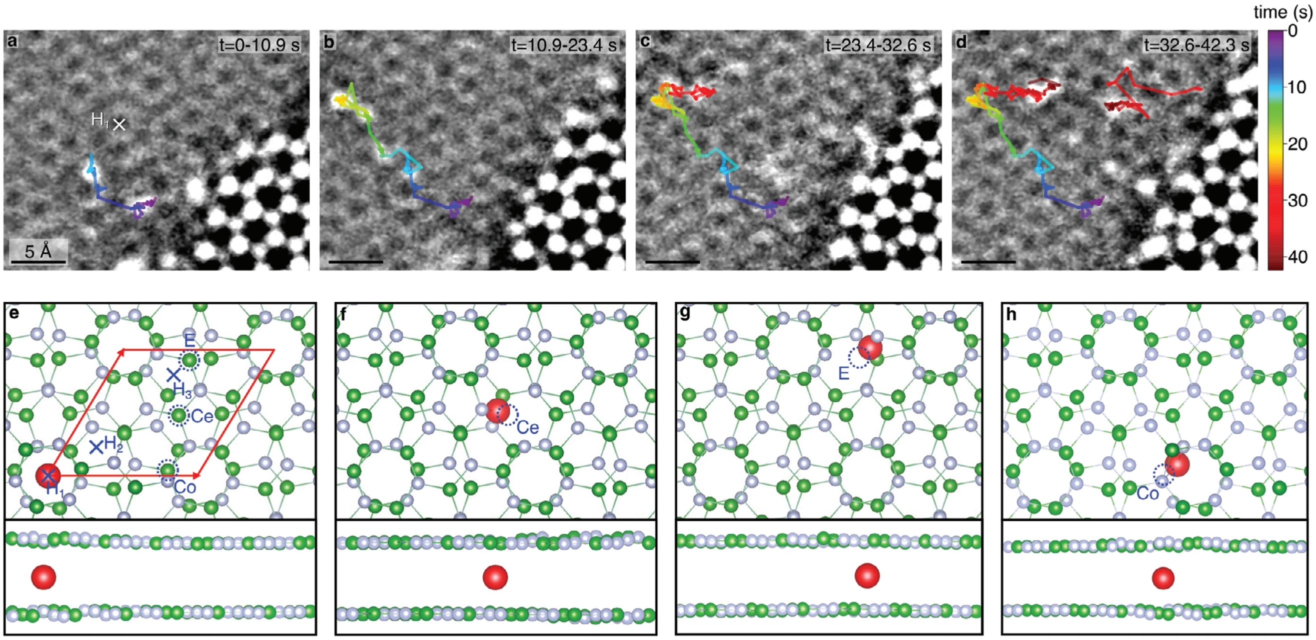

Figure 4. Atomic motion in BN–BN interface. a–d) Atomic trajectories recorded in the time intervals t = 0–10.9, 10.9–23.4, 23.4–32.6, and 32.6–42.3 s, respectively. The trajectories for previous intervals are included in later ones (data from Video S6, Supporting Information). In (d), another W atom emerges from the WSe_2 edge. e–h) DFT-relaxed atomic structures of a W atom intercalated between two BN layers. For simplicity, this simulation only includes one layer on either side of the interface. Green, silver, and red spheres denote the B, N, and W atoms. e) A pristine BN/BN interface with characteristic hollow and lattice sites indicated in blue. The red arrows indicate the moiré unit cell (see Experimental Section for the construction). In a pristine BN bilayer, the W atom tends to sit at H_1. f–h) W atom stable sites in the presence of a Ce (f), E (g), or Co (h) defect. All three configurations show that sites near the B vacancy are preferred over H_1.

Figure 5d shows results from DFT calculations that predict the most stable site for W atoms on a pristine BN surface is in the hollow site, as minimal orbital overlap gives the maximum spacing for the adatom. B vacancies are a far more stable site for W adatoms (Figure 5e). Our experimental observation that W atoms occupy lattice sites on the BN is consistent with the importance of defects in the BN layer in determining pinning sites.

In these calculations, the thickness of BN does not affect the results. This is shown in Figure S7g,h (Supporting Information) where we find a similar stable site for a W atom on a pristine surface and at a B vacancy, whether the BN thickness is monolayer or bilayer. Furthermore, N vacancies behave similarly to B. Figure S7i (Supporting Information) shows that N vacancies lead to stable sites with even higher binding energy (we calculate defect formation energies of 6.75 and 9.65 eV for W in a B or N vacancy, respectively, on monolayer BN; details in Experimental Section). This suggests that W atoms are more likely to bind to a B vacancy compared to an N vacancy at equilibrium conditions although local perturbations may alter the situation. While we cannot identify a specific lattice site on the BN surface as N or B, experimentally we also do not observe a preference for either of the B or N lattice sites.

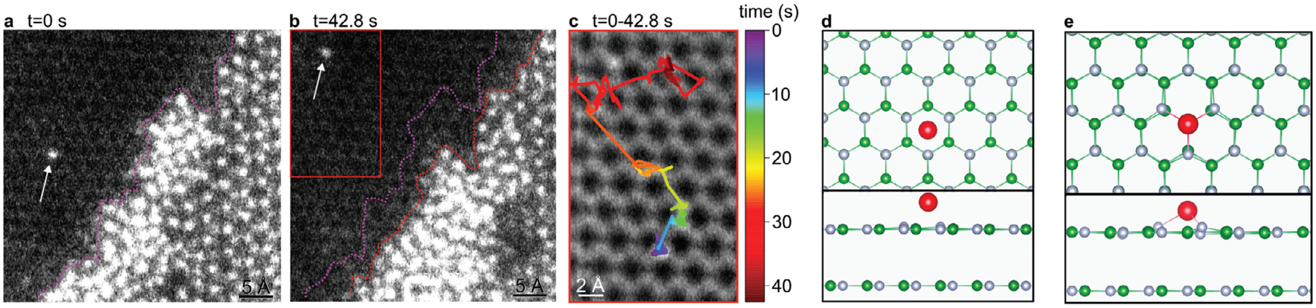

Figure 5. W diffusion at the BN/vacuum interface. a,b) First and last frame, respectively, from Video S7 (Supporting Information), showing a W atom on the surface of ≈2 nm BN. The purple and red dotted line indicates the edge of the WSe_2 layer at the start and end of the video. The tracked atom is indicated with a white arrow. c) STEM-HAADF obtained by summing 197 frames of the video. The trajectory of the W atom is shown on top. d) DFT-relaxed structure showing the most stable position for a W atom on a pristine BN bilayer. e) DFT relaxed structure of W near a B vacancy on a BN surface. For computational efficiency, the BN in the calculation is two monolayers thick.

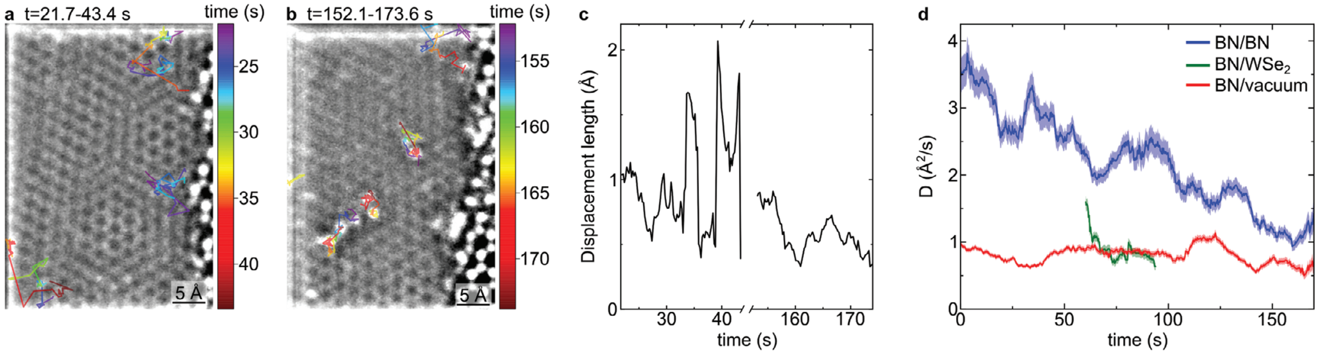

Figure 6. Time-dependent diffusion properties. a) All atomic trajectories in a 21.7 s time interval (corresponding to 100 images) starting at $t = 21.7$ s. b) All atomic trajectories in a 21.7 s time interval starting at $t = 152.1$ s. c) A running average of the displacement length of the atomic trajectories shown in (b, c). The running average is constructed by, first, averaging the displacement length of all atoms in a given time step, and, second, performing a running average over 10 time steps (2.17 s). The larger spikes at, e.g. t = 34 and 40 s are due to the large displacements at occurring at these times (see panel (b)). d) The W diffusion coefficient averaged across all tracked atoms and plotted against time for the BN/BN, BN/vacuum, and BN/WSe_2 interface, respectively. The diffusion coefficient was calculated using a co-variance-based estimator[35] on a rolling time-window of 15 s. The time used for plotting is the start of each window. The shaded areas in each plot correspond to the error bars. We note that the data from the BN/WSe_2 interface is obtained by manual tracking of atoms since automatic tracking of an extra W atom on a background lattice of WSe_2 is challenging. See Experimental Section for details.

6. Statistics of the Atomic Motion at Each Interface

Having shown qualitatively that W atoms appear to move through displacements between defect sites, we focus now on a quantitative analysis of the time-dependence of this behavior. This quantitative analysis simplifies considerably if the diffusion coefficient does not depend on direction. Therefore, we first investigated the diffusion isotropy, see Figures S10–S13 (Supporting Information). We found that the diffusion is isotropic except for the shortest displacements, less than one atomic spacing. These display some degree of anisotropy aligned with the axes of the image, implying that the result is due to measurement artifacts (see caption Figure S10, Supporting Information). We further note that we do not find any evidence that the motion is affected by the electron beam scanning direction.

Since defects are continuously produced by the electron beam during the experiment, we expect a gradual increase in the frequency with which diffusing atoms are trapped on defects. This lowers the diffusion coefficient over time. To test this hypothesis, we next investigate the time-dependent diffusion coefficient.

We performed experiments where we acquired data for ≈170 s from approximately the same area of a sample, by minimizing sample drift, and measured the diffusivity of the atoms in these videos. For this data, we define t = 0 as the time when a pristine area on the sample is first imaged. For the BN/BN interface we observe a marked decrease in W atom diffusivity. This is visible, for example, in data such as Video S8 (Supporting Information), which was recorded from t = 0. Such a trend is not apparent for the BN/WSe_2 and BN/vacuum interfaces as we will show and discuss below.

At the start of an experiment, tracking single atoms is challenging because their displacements between video frames can be large before many defects have been formed by the electron beam (Figure S14, Supporting Information). Shortly afterward, **Figure** 6a shows W atom trajectories from early times (100 frames, corresponding to 21.7 s) of an experiment while Figure 6a shows W atom trajectories from the last 21.7 s from the same experiment. We find that their average displacement length decreases over time (Figure 6c).

We then averaged across all trajectories recorded to find the overall behavior of W atoms at each interface. The diffusion coefficient, D, is optimally estimated using a co-variance based estimator[35] (Experimental Section). We used this method on all displacements observed within a rolling time-window of 15 s to elucidate the time-dependence of the diffusion coefficient.

Figure 6d shows the W diffusion coefficient plotted against time for each interface. For the BN/BN interface, D decreases over time, starting at a value of 3.5 $Å^2\ s^{-1}$ at t = 0 s and ending at a value of 1.5 $Å^2\ s^{-1}$ at t = 150 s. We expect the initial value of 3.5 $Å^2\ s^{-1}$ is a lower bound of D because we find that the W atoms initially undergo large displacements which are challenging to track. When several atoms are present near each other this would result in an underestimation of their displacements with the nearest-neighbor tracking algorithm (see Experimental Section) we used.

Imaging beyond ≈150 s results in the loss of BN/BN moiré image intensity, see Figures S15–S17 (Supporting Information). This indicates damage in the BN structure, and hence is consistent with the hypothesis that the decreasing diffusion coefficient is due to the continuous introduction of defects until the electron beam drills a hole through the sample with W atoms agglomerated along the edges of the hole—see in particular Figures S15 and S16 (Supporting Information). Such an interpretation is supported by literature. It is known that electron beam generated defects are not created uniformly through the thickness of a 2D material, but form more readily at the bottom surface.[30] TEM experiments in literature with BN have also shown that BN tends to be removed in a layer-by-layer fashion from the bottom surface with ≈$6 \cdot 10^6$ electrons $Å^{-2}$ needed for the removal of a layer.[36] We use a beam current of 50 pA to scan a 4 × 4 nm area, giving a dose rate of $2 \cdot 10^5$ electrons $Å^{-2}\ s^{-1}$. Thus, we need ≈30 s to remove a BN monolayer, fitting well with our observation of 150 s needed to etch through 2 nm of BN, corresponding to six monolayers of BN.

In addition, experiments at 60 kV show that degradation of the BN/BN interface and formation of W vacancies in bulk WSe_2 occurs at significantly longer time scales. At 60 kV, imaging beyond 400–600 s is needed before any noticeable BN/BN moiré intensity loss (Figures S18 and S19 and Video S9, Supporting Information). Imaging the BN/WSe_2 interface, a pristine region was imaged for almost 400 s before the formation of a W vacancy (Figure S20 and Video S10, Supporting Information). Thus, defect formation is highly dependent on electron beam energy, and use of lower electron beam energies may be a viable strategy for observing a sample without significant defect formation or modification.

At the BN/vacuum interface, the diffusion coefficient for W atoms fluctuates around a value of 0.8 Å^2 s^{-1}. In literature, the diffusivity of intercalated atoms in vdW materials has been shown to increase with interlayer distance.[37,38] Hence, intuitively one would expect that atoms diffusing on the free surface of BN would display faster diffusion compared to atoms diffusing in a vdW-bonded interface. We believe that two factors may account for the lower diffusivity at the BN/vacuum interface compared to the BN/BN interface. First, polymeric contamination is ubiquitous on the surface of 2D materials samples that have been transferred to TEM grids using polymer handles.[39] Such carbon-containing contamination is challenging to image through a multilayer due to its low atomic mass and is known to pin atoms diffusing on the surface of 2D materials.[34] Second, the data from the BN/vacuum interface comes from a sample where W atoms diffused on the bottom side of the BN with respect to electron beam direction. The bottom surface of a 2D material is more prone to electron beam-induced defects, since atoms can be removed more easily by direct knock-on damage.[29] Thus, the surprising result that the diffusion coefficient of W atoms at the BN/vacuum interface is significantly smaller than that of W atoms at the BN/BN interface suggests that the diffusion properties are less affected by interlayer distances, and more strongly depend on the defect concentration and the presence of contamination on the sample.

Finally, for the BN/WSe_2 interface, we find that W atoms are released from the WSe_2 lattice typically after at least 60 s of imaging. The start of each recorded trajectory is therefore set to $t = 60$ s. D appears to be decreasing initially and then fluctuates around a value of ≈0.8 Å^2 s^{-1}, the same as the diffusion coefficient of W atoms at the BN/vacuum interface. This may be the result of the amount of imaging typically needed to release W atoms from bulk WSe_2, where by the time W is released the interface is already markedly damaged.

Combining information for all three interfaces, we conclude that the comparative D values and their variation with time are consistent with atomic motion dominated by impurities and defects that are created by the electron beam at the interface.

7. Conclusion

We have quantified the diffusion of W atoms at the BN/vacuum, BN/BN, and BN/WSe_2 interfaces with atomic resolution imaging of single atoms through several atomic layers of BN, measuring not only diffusion parameters but also atomistic diffusion pathways. Our results show that the diffusion properties of W atoms in vdW-bonded interfaces are tunable and highly affected by defects at the interface. We determine this by directly visualizing trapping sites during the diffusion and comparing with expectations from DFT calculations. We further quantify diffusion properties and find a strong impact of defect concentration on the diffusion coefficient of W atoms at the BN/BN interface. This results in a time-dependent diffusion coefficient as a result of defects added during STEM imaging at 200 kV acceleration voltage. In addition, we have performed experiments with a 60 kV acceleration voltage showing the formation of defects at a significantly slower rate. The strong dependence on defects suggests that the vdW crystal quality is very important to consider when designing intercalation and diffusion processes.

We anticipate that this work will offer strategies for visualizing diffusion and atomic interactions within vdW gaps. Any relatively heavy atom, e.g., Ta, W, Pt, etc., can be imaged, and interactions between atoms with particular properties such as magnetic can be examined. It is also possible to perform the experiments in a TEM sample holder capable of heating or cooling the sample, to enable measurements say above and below a magnetic critical temperature. The vdW heterostructures we have examined, with their relatively thick insulating layers of ≈2 nm BN, are compatible with electrical property measurements, they permit simultaneously measuring atomic structure and electrical properties. Having shown that imaging with a lower electron beam energy significantly reduces defect formation, the use of controlled electron beam dosing and low-energy electrons will enable small modifications to be made and changes to electrical properties measured.

In addition, the use of other 2D materials for encapsulation, especially if composed of light elements, allows further possibilities. A conductive material like graphene enables quantification of the diffusion behavior as a function of electrical current and possibly atomic-level measurements of electromigration. Use of an anisotropic material like phosphorene enables studying directional diffusion. Using 2D materials with specific defect types, such as grain boundaries, allows directly evaluating the effect of such defects on diffusion and trapping. Finally, we highlight that novel TEM methods could aid in such experiments. Progress in image de-noising and machine learning for atom tracking could facilitate experiments at high frame-rates or low electron energies,[40] and electron beam programming and automated experiments could be used to create specific defects at predetermined sites.[41] This includes the possibility of engineering arrays of atoms by seeding defects in determined positions. The ability to image individual atoms with good time and space resolution therefore offers exciting prospects for future progress in atomic-level material design.

8. Experimental Section

Sample Fabrication: WSe_2 crystals were purchased from HQ Graphene. BN and WSe_2 crystals were exfoliated onto an SiO_2 (90 nm)/Si substrate and suitable flakes were identified using optical contrast. The vdW heterostructures were fabricated using a sequential pick-up of the top BN and monolayer WSe_2, and releasing this BN/WSe_2 heterostructure on the bottom BN. A poly(bisphenol A carbonate) (PC)-film-covered polydimethylsiloxane (PDMS) stamp on a glass slide for the transfers was used. Finally, the heterostructures were transferred to SiN/Si TEM grids, purchased from Norcada, Canada, using wedging transfer.[42]

STEM: HAADF-STEM imaging was performed in a Titan Themis Z G3 Cs-corrected S/TEM with a beam current of 50 pA. All data in the main text were obtained with an acceleration voltage of 200 kV and a frame time of 0.217 s (512 × 512 pixels with a dwell time of 500 ns). In Figures S17–S19 (Supporting Information) data obtained with beam current of 50 pA, acceleration voltage of 60 kV, images with 512 × 512 pixels, and dwell times as listed in the captions are shown. The Supporting Information contains details on all Videos (video length, sample type, scale). Raw data for all Videos (Supporting Information) can be downloaded at.[43]

Atom Tracking: Raw videos were drift-corrected using a rigid registration tracking scheme[44] using ImageJ. Subsequently, single atoms were tracked using TrackMate[45] which is a plugin to ImageJ. The nearest-neighbor tracker which links the nearest atoms in subsequent images, with a maximum linking distance of 1 nm was used.

If there are several atoms present within the maximum linking distance this can create false linking between atoms. To minimize these events, areas in the data with a large density of atoms were excluded and/or additional manual filtering of tracks to eliminate false links was performed. The procedure for detecting and tracking atoms using TrackMate is shown in Figure S21 (Supporting Information). To verify the approach, the time-dependent diffusion coefficient of the full data-set was compared with the diffusion coefficient obtained from data with a low concentration of atoms in Figure S22 (Supporting Information). Both data sets showed similar values for diffusion coefficients and similar time-dependent behavior, showing that this approach was valid.

It was challenging for TrackMate to identify the moving W atoms on background of a WSe_2 lattice, i.e., at the BN/WSe_2 interface. For this interface, the W atoms were manually tracked using imageJ. For the pinning site statistics of the BN/WSe_2 interface shown in Figure 3f images such as the one shown in Figure 3e were overlaid with a voronoi lattice which defines the spatial extent of each W, Se_2, and H site and W atoms that fall within each voronoi cell were counted.

Calculation of Diffusion Coefficients: Let $\mathbf{r}^{(j)}(t) = \{x^{(j)}(t), y^{(j)}(t)\}$ denote the trajectory of Atom #*j*. Individual atoms from videos obtained with HAADF-STEM imaging with a frame time of $\Delta t = 0.217$ s were tracked. This resulted in time-lapse recorded coordinates on the trajectory, $r_n^{(j)} = r^{(j)}(t_n)$ where $t_n = n\Delta t$, $n = 0, 1, \ldots, N$. With this notation, a trajectory is built by *N* consecutive displacements.

The zero-point in time for the BN/BN and BN/vacuum interface was the start of a new video being recorded in an area that had not previously been imaged. For the BN/WSe_2 interface, the zero-point in time was the start of each trajectory. It was further estimated that ≈60 s was required to observe moving W atoms when imaging a bulk area, and therefore the time-dependent diffusion coefficient of W atoms at the BN/WSe_2 interface was plotted starting from t = 60 s (Figure 6d).

The time-dependent diffusion coefficient was estimated using CVE, the co-variance based estimator of ref. [35], on a rolling time window of 15 s. All displacements in *x* and *y* occurring in a given time interval were used for the estimate. The window was then moved one time-step, $\Delta t = 0{,}217$ s, and the calculation repeated. CVE estimates the diffusion coefficient with [35, Equation (14)]

$$D = \frac{\overline{(\Delta x_n)^2}}{2\Delta t} + \frac{\overline{\Delta x_n \Delta x_{n+1}}}{\Delta t} \tag{1}$$

where $\overline{(\ldots)}$ denotes the average over all displacements Δx_n within a given time window. The error bars in Figure 6d are given by the square root of the variance of *D*, which is estimated with [35, Equation (17)]

$$\mathrm{var}(D) = D^2\left(\frac{6 + 4\epsilon + 2\epsilon^2}{N_{\mathrm{win}}} + \frac{4(1+\epsilon)^2}{N_{\mathrm{win}}^2}\right) \tag{2}$$

where N_{win} is the number of displacements in a given time window and $\epsilon = \sigma^2/D\Delta t - 2R$. Here, *R* is the so-called motion blur coefficient, and σ^2 is the variance of the localization error. The images are 512 × 512 pixels large, and the size of one W atom was estimated to be ≈20 × 20 pixels for the magnification that was used. Hence, $R = 20/512 \approx 0.04$ was estimated. The variance σ^2 was estimated by [35, Equation (15)]

$$\sigma^2 = R\overline{(\Delta x_n)^2} + (2R-1)\overline{\Delta x_n \Delta x_{n+1}} \tag{3}$$

DFT Calculations: The density functional theory (DFT) calculations were performed using the Vienna ab initio simulation package (VASP)[46,47] within the generalized gradient approximation (GGA) with Perdew–Burke–Ernzerhof (PBE)[48] functional and a plane-wave cut-off of 520 eV and Γ point integration in reciprocal space.[49] Dispersion correction was described by the Grimme's DFT-D2 method[50] and the global scaling factor was set to $s_6 = 0.15$ to find the best match of spacing between the BN layers. The rev-vdW-DF2, optB88, and r2scan functionals were also tested and only a 2% deviation was found in the interlayer spacing compared to that found with Grimme's D2 method, see Figure S23 (Supporting Information). For the BN/WSe_2 interface, Grimme's DFT-D2 method was also employed to find an interlayer distance of 5.1 Å. However, the experimentally measured interlayer distance for a BN/WSe_2 heterostructure was ≈0.9 Å larger than that predicted by DFT.[26] Therefore, the larger interlayer spacing was also tested, see Figure S7b (Supporting Information).

For simplicity, for the BN/WSe_2 interface a BN/WSe_2 heterostructure without any rotation between the two crystals was simulated. Also for simplicity, only B vacancies at the BN/BN interface were considered: based on the other calculations similar results were expected if N vacancies were added.

The bilayer BN moiré superlattice was constructed with a twisting angle of 21.79° instead of the measured exact 23.9°, for the purpose of finding the integer solutions of the moiré lattice parameters.[51] The moiré unit cell consists of 14 B and 14 N atoms, from which a 3 × 3 supercell was built to minimize the interactions between a defect and its images. For the WSe_2/BN bilayer, uniform strain was introduced on the BN lattice and a 3 × 3 WSe_2 and 4 × 4 BN commensurate supercell was constructed. A slab geometry with a 2 nm vacuum layer perpendicular to the atomic plane was used to minimize the interactions between images. All atoms in the supercell were allowed to relax until the residual force per atom was less than 0.01 eVÅ^{-1}.

To better estimate how different vacancy type affects the diffusion behavior of W, the defect formation energy for a W atom on top of either B or N vacancy was calculated. The defect formation energy, E_{f}, is given by[52]

$$E_{\mathrm{f}}(W_{\mathrm{B,\,N}}) = E(W_{\mathrm{B,\,N}}) - E_{\mathrm{perf}} + \mu_{\mathrm{B,\,N}} - \mu_{\mathrm{W}} + Q(E_{\mathrm{F}} + E_{\mathrm{v}}) \tag{4}$$

where $E(W_{\mathrm{B,\,N}})$ is the total energy of a relaxed BN supercell with a W atom and a B or N vacancy, E_{perf} is the total energy of a perfect BN supercell, $\mu_{\mathrm{B,\,N}}$ is the chemical potential of B or N, μ_{W} is the chemical potential of W, *Q* is the charge state of the vacancy, E_F is the Fermi energy with $0 < E_F < E_{\mathrm{gap}}$, and E_{v} is the energy of the top of the valence band. It was noted that the calculation of defect formation energies was a non-trivial problem in gapped materials, and therefore, for simplicity the charged defect was not considered, i.e. $Q = 0$. The most important variables were the chemical potentials. In the calculation, the elementary limit was chosen, meaning that $\mu_{\mathrm{B,\,N}}$ equal to the elementary limit was set for a B or N-rich case, respectively. Therefore, combining $\mu_{\mathrm{B}} + \mu_{\mathrm{N}} = E_{\mathrm{perf}}$, enabled solving the chemical potential $\mu_{\mathrm{B,\,N}}$ in different conditions and thus the defect formation energy.

Supporting Information

Supporting Information is available from the Wiley Online Library or from the author.

Acknowledgements

This work was partially supported by the U.S. Department of Energy, Office of Science, Basic Energy Sciences (BES), Materials Sciences and Engineering Division under FWP ERKCK47 "Understanding and Controlling

Entangled and Correlated Quantum States in Confined Solid-state Systems Created via Atomic Scale Manipulation." J.D.T. was partially supported by the Army Research Office MURI (Ab-Initio Solid-State Quantum Materials) grant number W911NF-18-1-0431. P.N. is a Moore Inventor Fellow through Grant GBMF8048 from the Gordon and Betty Moore Foundation. Calculations were performed using resources from the Department of Defense High Performance Computing Modernization program (HPCMP). Additional calculations were performed using resources of the National Energy Research Scientific Computing Center, a DOE Office of Science User Facility, as well as resources at UCLA. Transmission electron microscopy was performed using the MIT.nano Characterization Facilities. Y.W. acknowledges support from the Chinese Academy of Sciences (Nos. YSBR047 and E2K5071). H.F. acknowledges support from the Strategic Programme Excellence Initiative at the Jagiellonian University. E. P. acknowledges support from a Mathworks Fellowship. K.W. and T.T. acknowledge support from the JSPS KAKENHI (Grant Numbers 20H00354, 21H05233 and 23H02052) and World Premier International Research Center Initiative (WPI), MEXT, Japan.

Author Contributions

J.D.T. fabricated the samples, performed the STEM experiments and analyzed the data. Y.W. performed the DFT simulations. H.F. advised on the quantitative diffusion analysis. K.W. and T.T. grew the BN crystals. E.P. acquired overview STEM and TEM images of the samples. P.N. and F.M.R. supervised the project. J.D.T. wrote the manuscript with the input of all co-authors.

Conflict of Interest

The authors declare no conflict of interest.

Data Availability Statement

The data that support the findings of this study are openly available in Zenodo at https://doi.org/10.5281/zenodo.11491425, reference number 11491426.

Keywords

2D materials, diffusion, DFT calculations, transmission electron microscopy, van der Waals heterostructures

Received: March 18, 2024
Revised: July 15, 2024

---

[1] Y.-C. Lin, D. O. Dumcenco, Y.-S. Huang, K. Suenaga, *Nat. Nanotechnol.* **2014**, *9*, 391.
[2] X. Zhang, T. H. Choudhury, M. Chubarov, Y. Xiang, B. Jariwala, F. Zhang, N. Alem, G.-C. Wang, J. A. Robinson, J. M. Redwing, *Nano Lett.* **2018**, *18*, 1049.
[3] W. Spear, P. L. Comber, *Solid State Commun.* **1975**, *17*, 1193.
[4] S. Wang, A. Robertson, J. H. Warner, *Chem. Soc. Rev.* **2018**, *47*, 6764.
[5] Y. Wu, D. Li, C.-L. Wu, H. Y. Hwang, Y. Cui, *Nat. Rev. Mater.* **2023**, *8*, 41.
[6] M. Rajapakse, B. Karki, U. O. Abu, S. Pishgar, Md. R. K. Musa, S. M. S. Riyadh, M. Yu, G. Sumanasekera, J. B. Jasinski, *npj 2D Mater. Appl.* **2021**, *5*, 30.
[7] D. Rhodes, S. H. Chae, R. Ribeiro-Palau, J. Hone, *Nat. Mater.* **2019**, *18*, 541.
[8] Y. Liu, N. O. Weiss, X. Duan, H.-C. Cheng, Y. Huang, X. Duan, *Nat. Rev. Mater.* **2016**, *1*, 1.
[9] K. Novoselov, o. A. Mishchenko, o. A. Carvalho, A. C. Neto, *Science* **2016**, *353*, aac9439.
[10] K. S. Burch, D. Mandrus, J.-G. Park, *Nature* **2018**, *563*, 47.
[11] M. Gibertini, M. Koperski, A. F. Morpurgo, K. S. Novoselov, *Nat. Nanotechnol.* **2019**, *14*, 408.
[12] D. M. Kennes, M. Claassen, L. Xian, A. Georges, A. J. Millis, J. Hone, C. R. Dean, D. N. Basov, A. Pasupathy, A. Rubio, *Nat. Phys.* **2021**, *17*, 155.
[13] S.-Z. Yang, W. Sun, Y.-Y. Zhang, Y. Gong, M. P. Oxley, A. R. Lupini, P. M. Ajayan, M. F. Chisholm, S. T. Pantelides, W. Zhou, *Phys. Rev. Lett.* **2019**, *122*, 106101.
[14] Y. Gan, L. Sun, F. Banhart, *Small* **2008**, *4*, 587.
[15] J. Hong, Y. Pan, Z. Hu, D. Lv, C. Jin, W. Ji, J. Yuan, Z. Zhang, *Nano Lett.* **2017**, *17*, 3383.
[16] H. Li, S. Wang, H. Sawada, G. G. D. Han, T. Samuels, C. S. Allen, A. I. Kirkland, J. C. Grossman, J. H. Warner, *ACS Nano* **2017**, *11*, 3392.
[17] R. Ishikawa, R. Mishra, A. R. Lupini, S. D. Findlay, T. Taniguchi, S. T. Pantelides, S. J. Pennycook, *Phys. Rev. Lett.* **2014**, *113*, 155501.
[18] M. Längle, K. Mizohata, C. Mangler, A. Trentino, K. Mustonen, E. H. Åhlgren, J. Kotakoski, *Nat. Mater.* **2024**, *23*, 762.
[19] O. Dyck, S. Kim, S. V. Kalinin, S. Jesse, *Appl. Phys. Lett.* **2017**, *111*, 113104.
[20] T. Susi, *Chem. Commun.* **2022**, *58*, 12274.
[21] S. J. Haigh, A. Gholinia, R. Jalil, S. Romani, L. Britnell, D. C. Elias, K. S. Novoselov, L. A. Ponomarenko, A. K. Geim, R. Gorbachev, *Nat. Mater.* **2012**, *11*, 764.
[22] A. V. Kretinin, Y. Cao, J. S. Tu, G. L. Yu, R. Jalil, K. S. Novoselov, S. J. Haigh, A. Gholinia, A. Mishchenko, M. Lozada, T. Georgiou, C. R. Woods, F. Withers, P. Blake, G. Eda, A. Wirsig, C. Hucho, K. Watanabe, T. Taniguchi, A. K. Geim, R. V. Gorbachev, *Nano Lett.* **2014**, *14*, 3270.
[23] J. J. Schwartz, H.-J. Chuang, M. R. Rosenberger, S. V. Sivaram, K. M. McCreary, B. T. Jonker, A. Centrone, *ACS Appl. Mater. Interfaces* **2019**, *11*, 25578.
[24] F. Pizzocchero, L. Gammelgaard, B. S. Jessen, J. M. Caridad, L. Wang, J. Hone, P. Bøggild, T. J. Booth, *Nature Commun.* **2016**, *7*, 11894.
[25] H. Y. Lee, S. Sarkar, K. Reidy, A. Kumar, J. Klein, K. Watanabe, T. Taniguchi, J. M. LeBeau, F. M. Ross, S. Gradecak, *Nat. Commun.* **2022**, *13*, 5000.
[26] A. P. Rooney, A. Kozikov, A. N. Rudenko, E. Prestat, M. J. Hamer, F. Withers, Y. Cao, K. S. Novoselov, M. I. Katsnelson, R. Gorbachev, S. J. Haigh, *Nano Lett.* **2017**, *17*, 5222.
[27] P. Hartel, H. Rose, C. Dinges, *Ultramicroscopy* **1996**, *63*, 93.
[28] M. J. Skaug, J. Mabry, D. K. Schwartz, *Phys. Rev. Lett.* **2013**, *110*, 256101.
[29] H.-P. Komsa, J. Kotakoski, S. Kurasch, O. Lehtinen, U. Kaiser, A. V. Krasheninnikov, *Phys. Rev. Lett.* **2012**, *109*, 035503.
[30] J. Kotakoski, C. H. Jin, O. Lehtinen, K. Suenaga, A. V. Krasheninnikov, *Phys. Rev. B* **2010**, *82*, 113404.
[31] J. Zhang, R. Sun, D. Ruan, M. Zhang, Y. Li, K. Zhang, F. Cheng, Z. Wang, Z.-M. Wang, *J. Appl. Phys.* **2020**, *128*, 100902.
[32] T. A. Bui, G. T. Leuthner, J. Madsen, M. R. A. Monazam, A. I. Chirita, A. Postl, C. Mangler, J. Kotakoski, T. Susi, *Small* **2023**, *19*, 2301926.
[33] F. İyikanat, H. Sahin, R. T. Senger, F. M. Peeters, *APL Mater.* **2014**, *2*, 092801.
[34] R. Zan, U. Bangert, Q. Ramasse, K. S. Novoselov, *Nano Lett.* **2011**, *11*, 1087.
[35] C. L. Vestergaard, P. C. Blainey, H. Flyvbjerg, *Phys. Rev. E* **2014**, *89*, 022726.

[36] S. M. Gilbert, G. Dunn, A. Azizi, T. Pham, B. Shevitski, E. Dimitrov, S. Liu, S. Aloni, A. Zettl, *Sci. Rep.* **2017**, *7*, 1.

[37] H. D. Yoo, Y. Liang, H. Dong, J. Lin, H. Wang, Y. Liu, L. Ma, T. Wu, Y. Li, Q. Ru, Y Jing, Q An, W. Zhou, J. Guo, J. Lu, S. T. Pantelides, X. Qian, Y. Yao, *Nat. Commun.* **2017**, *8*, 339.

[38] K. D. Rasamani, F. Alimohammadi, Y. Sun, *Mater. Today* **2017**, *20*, 83.

[39] Y.-C. Lin, C.-C. Lu, C.-H. Yeh, C. Jin, K. Suenaga, P.-W. Chiu, *Nano Lett.* **2012**, *12*, 414.

[40] J. M. Ede, *Mach. Learn.: Sci. Technol.* **2021**, *2*, 011004.

[41] S. V. Kalinin, D. Mukherjee, K. Roccapriore, B. J. Blaiszik, A. Ghosh, M. A. Ziatdinov, A. Al-Najjar, C. Doty, S. Akers, N. S. Rao, J. C. Agar, S. R. Spurgeon, *npj Comput. Mater.* **2023**, *9*, 227.

[42] J. D. Thomsen, T. Gunst, S. S. Gregersen, L. Gammelgaard, B. S. Jessen, D. M. A. Mackenzie, K. Watanabe, T. Taniguchi, P. Bøggild, T. J. Booth, *Phys. Rev. B* **2017**, *96*, 014101.

[43] J. D. Thomsen, F. M. Ross, Atomic resolution high-angle annular dark field scanning transmission electron microscopy imaging of WSe_2 encapsulated within hexagonal boron nitride. ZENODO **2024** note https://doi.org/10.5281/zenodo.11491425.

[44] N. Schneider, ImageJ script for drift correcting videos, https://github.com/NMSchneider/fixTranslation-Macro-for-ImageJ.

[45] D. Ershov, M.-S. Phan, J. W. Pylvänäinen, S. U. Rigaud, L. L. Blanc, A. Charles-Orszag, J. R. W. Conway, R. F. Laine, N. H. Roy, D. Bonazzi, G. Duménil, G. Jacquemet, J.-Y. Tinevez, *Nat. Methods* **2022**, *19*, 829.

[46] G. Kresse, J. Hafner, *Phys. Rev. B* **1993**, *47*, 558.

[47] G. Kresse, D. Joubert, *Phys. Rev. B* **1999**, *59*, 1758.

[48] J. P. Perdew, K. Burke, M. Ernzerhof, *Phys. Rev. Lett.* **1996**, *77*, 3865.

[49] G. Kresse, J. Furthmüller, *Phys. Rev. B* **1996**, *54*, 11169.

[50] S. Grimme, *J. Chem. Phys.* **2006**, *27*, 1787.

[51] M. Feuerbacher, *Acta Cryst. A* **2021**, *77*, 460.

[52] Y. Wang, W. Windl, *J. Appl. Phys.* **2021**, *129*, 075703.